Observation of a two-dimensional Fermi surface and Dirac dispersion in $YbMnSb_2$

Robert Kealhofer,[1,2] Sooyoung Jang,[1,2,3] Sinéad M. Griffin,[1,4] Caolan John,[1,2] Katherine A. Benavides,[5] Spencer Doyle,[1,2] T. Helm,[6] Philip J. W. Moll,[6] Jeffrey B. Neaton,[1,4] Julia Y. Chan,[5] J. D. Denlinger,[3] and James G. Analytis[1,2]

[1]*Department of Physics, University of California, Berkeley, California 94720, USA*
[2]*Materials Sciences Division, Lawrence Berkeley National Laboratory, Berkeley, California 94720, USA*
[3]*Advanced Light Source, Lawrence Berkeley National Laboratory, Berkeley, California 94720, USA*
[4]*Molecular Foundry, Lawrence Berkeley National Laboratory, Berkeley, California 94720, USA*
[5]*Department of Chemistry and Biochemistry, The University of Texas at Dallas, Richardson, Texas 75080, USA*
[6]*Max Planck Institute for Chemical Physics of Solids, Nöthnitzer Straße 40, 01187 Dresden, Germany*

(Received 4 August 2017; published 10 January 2018)

We present the crystal structure, electronic structure, and transport properties of the material $YbMnSb_2$, a candidate system for the investigation of Dirac physics in the presence of magnetic order. Our measurements reveal that this system is a low-carrier-density semimetal with a two-dimensional Fermi surface arising from a Dirac dispersion, consistent with the predictions of density-functional-theory calculations of the antiferromagnetic system. The low temperature resistivity is very large, suggesting that scattering in this system is highly efficient at dissipating momentum despite its Dirac-like nature.

DOI: 10.1103/PhysRevB.97.045109

I. INTRODUCTION

The coexistence of topological band structures and more conventional broken symmetry orders has yet to be investigated extensively, primarily due to the lack of suitable materials systems. As a result, several studies have focused on the structural family $RMnPn_2$, where R is a rare-earth metal and Pn is a pnictide (usually Sb or Bi) [1–6], due to the possible coexistence of protected band crossings and magnetic order on the Mn sublattice. The magnetic order is thought to be antiferromagnetic, breaking the spin degeneracy of the system, and it has been argued that this leads to crossings separated in energy in the band structure [7–9]. Two members of this family, $SrMnBi_2$ and $YbMnBi_2$, have been proposed as possible topological semimetals hosting magnetic order [3,10], but comparatively little work has investigated their Sb-based cousins [11,12]. We have synthesized a new member of this family, $YbMnSb_2$, and report here comprehensive transport and spectroscopic measurements. Evidence from Shubnikov-de Haas oscillations and angle-resolved photoemission spectroscopy (ARPES) suggest there is at least one two-dimensional (2D) Fermi surface of Dirac origin. The ARPES data are in agreement with density functional theory (DFT) calculations of the antiferromagnetic band structure, which indicates that $YbMnSb_2$ may therefore be a new topological material in the presence of magnetic order. However, despite the observation of quantum oscillations, the low temperature resistivity of these materials is large, suggesting that quantum and transport lifetimes have the same origin in these materials.

II. EXPERIMENT

A. Crystal synthesis and structure

Single crystals of $YbMnSb_2$ were synthesized using a tin-flux technique. Ytterbium (99.9%), manganese (99.95%), antimony (99.9999%), and tin (99.999%), all from Alfa Aesar, were mixed in the mole ratio 1:1:4:10 (Yb:Mn:Sb:Sn). The mixture was placed in an alumina crucible and sealed in an evacuated quartz ampule and then heated over 8 h to 1050 °C where it dwelled for 24 h. Next, the ampule was cooled to 600 °C over 100 h and then centrifuged to remove excess tin. This process yielded single crystals of approximately 1 mm × 1 mm × 0.05 mm.

The crystallographic parameters are listed in Table I and the atomic coordinates and displacement parameters are provided in Table II. The crystal structure is shown schematically in Fig. 1(a). Single crystals of $YbMnSb_2$ were cut to an appropriate size and mounted on a glass fiber using epoxy. The fiber was mounted on a Bruker D8 Quest Kappa single-crystal x-ray diffractometer with a Mo Kα IμS microfocus source ($\lambda = 0.71073$ Å) operating at 50 kV and 1 mA, a HELIOS optics monochromator, and a complementary metal-oxide-semiconductor technology-based detector. The Bruker program SADABS (multiscan method) was used to correct the collected data for absorption. A starting model of $YbMnSb_2$ was obtained using the intrinsic phasing method in SHELXT [13]. Atomic sites were refined anisotropically using SHELXL2014 [14]. Figure 1(b) shows a characteristic powder pattern (collected using Cu $K\alpha$ radiation on a Rigaku Ultima IV powder diffractometer) together with the simulated powder pattern, computed in VESTA [15]. Core-level spectroscopy on the MERLIN beamline (see Sec. IIC) confirms the divalent oxidation state of Yb [Fig. 1(c)].

$YbMnSb_2$ belongs to the tetragonal, centrosymmetric *P4/nmm* space group and is isotypic with the $HfCuSi_2$ structure type [16]. $YbMnSb_2$ does not exhibit an Mn deficiency that is observed in compounds of the same structure type with larger rare-earth elements, e.g., $LnMn_{1-x}Sb_2$ (Ln = La, Ce, Pr, Nd, or Sm) [17]. The independent confirmation of the $YbMnSb_2$ crystal structure allows for a first-principles calculation of the electronic band structure, which we consider next.

TABLE I. Crystallographic parameters.

Crystal type	$YbMnSb_2$
Space group	*P4/nmm*, #129
a, *c* (Å)	4.3215(17), 10.828(4)
V (Å^3)	202.22(17)
Z	2
Temperature (K)	300
θ range (°)	3.8–30.7
μ (mm^{-1})	38.93
Measured reflections	1085
Independent reflections	224
R_{int}	0.033
$\Delta\rho_{\max}$ (eÅ^{-3})	1.64
$\Delta\rho_{\min}$ (eÅ^{-3})	−3.56
GOF	1.27
$R_1(F)$[a]	0.033
wR_2[b]	0.060

[a] $R_1 = \Sigma||F_0| - |F_c||/\Sigma|F_0|$.
[b] $wR_2 = \{\Sigma[w(F_0^2 - F_c^2)^2]/\Sigma[w(F_0^2)^2]\}^{1/2}$.

B. Electronic structure

Using the lattice parameters using the measured structural data reported in Table I and Table II, we performed spin-polarized density functional calculations within the generalized gradient approximation (GGA) using the Vienna *ab initio* Simulation Package (VASP) [18,19]. We used the projector augmented wave (PAW) method, treating explicitly $5s, 5p, 4f$, and $6s$ for Yb; $3d$ and $4s$ for Mn; and $5s$ and $5p$ for Sb. We did not include Yb $4d$ electrons in our calculation. Wave functions were expanded in a plane-wave basis up to an energy cutoff of 600 eV. We used Monkhorst-Pack k-point grids of $10 \times 10 \times 4$ for Brillouin zone sampling [20]. Spin-orbit coupling was neglected except when computing the band structure in Fig. 2 and when identifying the magnetic easy axis. We used the PBE GGA functional [21] with Hubbard U corrections [22] for the Yb $4f$ states, where we used a U_{eff} of 4 eV. This value of U_{eff} was chosen to best reproduce the photoemission data, which placed the Yb $4f$ states at −0.6 eV below the Fermi energy. We did not include a Hubbard U for the Mn $3d$ electrons after tests indicated that such a U had no effect on the electronic structure near the Fermi level.

All calculations assumed antiferromagnetic (AFM) order for the spins on the Mn sites, with the two Mn ions in each cell having opposite spin. This AFM ordering was calculated to be 0.23 and 2.6 eV per formula unit lower in energy than ferromagnetic order and a non-spin-polarized calculation, respectively. We compute the magnetic easy axis to be in plane,

TABLE II. Atomic positions.

$YbMnSb_2$	Wyckoff site	x	y	z	U_{eq} (Å^2)
Yb	2*c*	1/4	1/4	0.72728(8)	0.0106(2)
Mn	2*a*	3/4	1/4	0	0.0115(6)
Sb 1	2*b*	3/4	1/4	1/2	0.0115(3)
Sb 2	2*c*	1/4	1/4	0.15995(12)	0.0099(3)

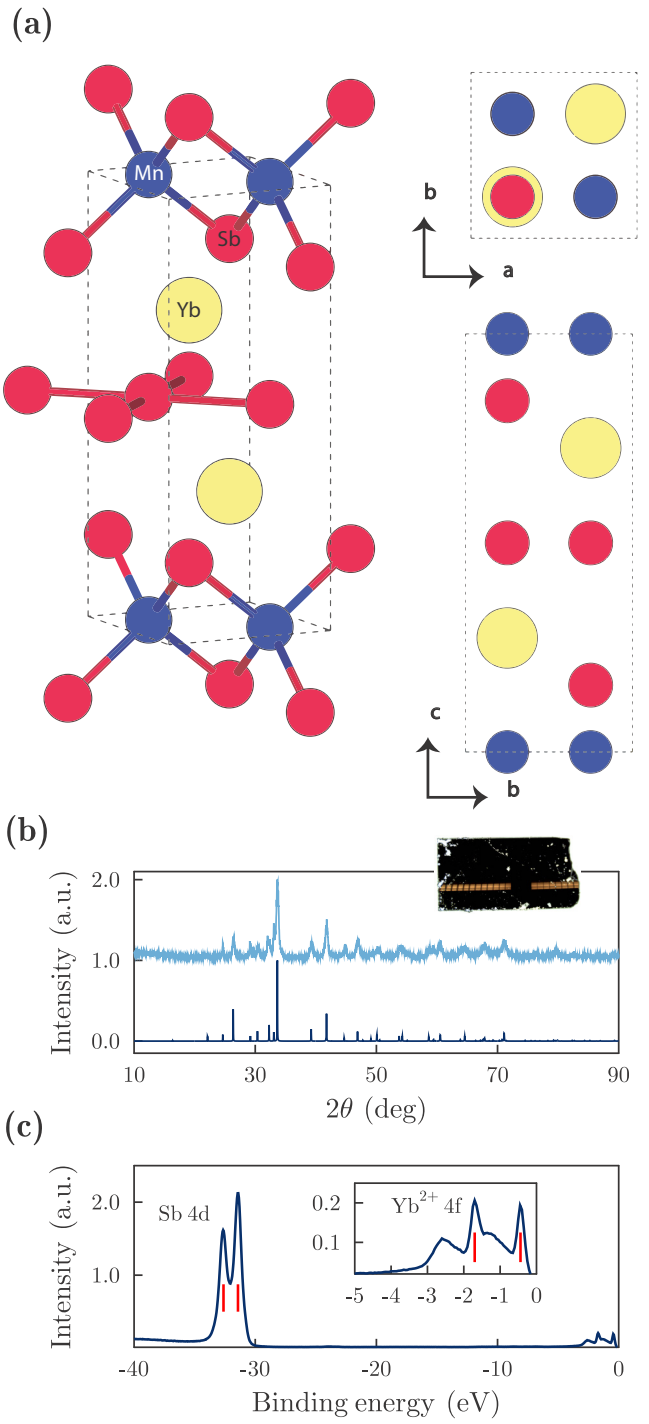

FIG. 1. The structure of $YbMnSb_2$. (a) Schematic of the $YbMnSb_2$ structure drawn in VESTA from single crystal x-ray diffraction data. $YbMnSb_2$ is isotypic with the $HfCuSi_2$ structure type. Here yellow is Yb, blue is Mn, and red is Sb. Perspective drawing (left) shows Sb planes and the tetrahedral coordination of Mn by Sb, the top right looks down the *c* axis, and the bottom right looks down the *a* axis. (b) Experimental powder pattern of $YbMnSb_2$ crystals (top trace) and expected powder pattern from Table I and Table II, simulated in VESTA. Inset: Millimeter-sized $YbMnSb_2$ crystal. Crystals are highly lustrous, as can be seen from the reflection of the fluorescent room lighting across the bottom of the crystal. (c) Core-level spectroscopy of $YbMnSb_2$ unambiguously indicates the 2+ oxidation state of Yb.

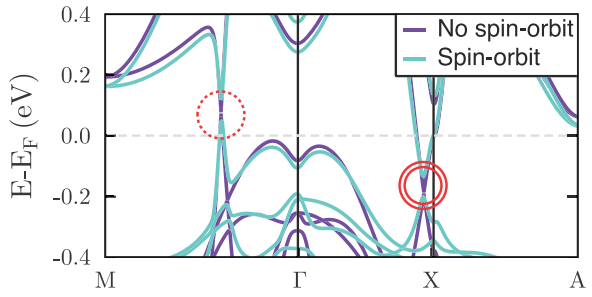

FIG. 2. Electronic structure of $YbMnSb_2$. Note the band crossings on the Γ-M and Γ-X lines, indicated with a dashed circle and a double circle, respectively.

and 1 meV/f.u. lower in energy than for out-of-plane spin orientations.

The band structure is shown in Fig. 2. Note the linear band crossings on the Γ-M and Γ-X lines. The calculated Fermi surface is displayed in Fig. 3 with a 10-meV energy resolution, showing 2D and 3D Fermi surface pockets. The Fermi level was chosen to achieve the approximate carrier concentration observed in transport measurements (see Fig. 5 and discussion). This corresponded to a shift of approximately −75 meV from the Fermi level shown in Fig. 2.

C. Angle-resolved photoemission spectroscopy

To experimentally investigate the electronic structure of $YbMnSb_2$, we performed ARPES measurements at the MERLIN beamline 4.0.3 of the Advanced Light Source, employing both linear horizontal and linear vertical polarization from an elliptically polarized undulator. The experiment used a Scienta R8000 electron spectrometer with 2D parallel detection of electron kinetic energy and angle in combination with a highly automated six-axis helium cryostat goniometer with

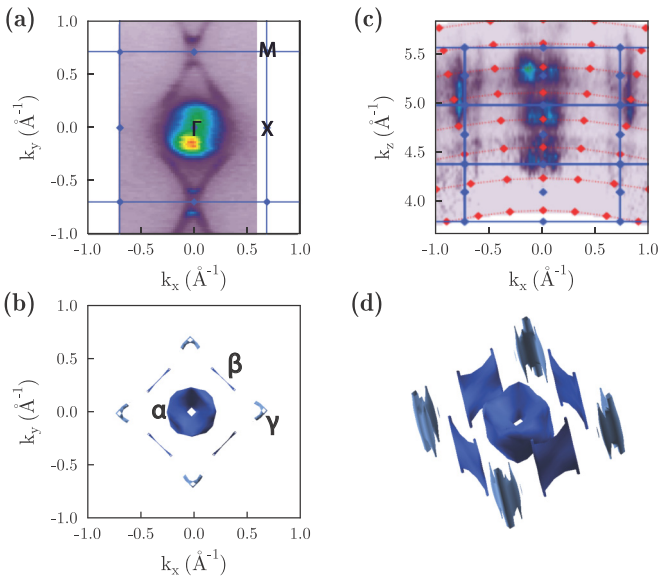

FIG. 3. (a) Fermi surface (FS) map at 78-eV photon energy. (b) Calculated FS with a 10-meV energy resolution. (c) Photon energy dependence of the ARPES intensity plot. (d) Perspective view of the calculated Fermi surface shown in (c).

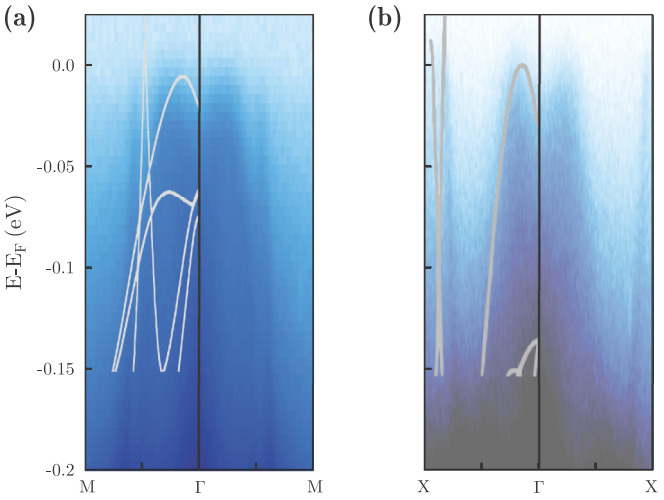

FIG. 4. ARPES intensity plot for (a) M-Γ-M and (b) X-Γ-X.

6 K base temperature operating in low 10^{-11} torr pressure. The energy resolution of these measurements was approximately 10–20 meV. These results are presented in Fig. 3 and Fig. 4.

D. DFT/ARPES comparison

Figure 3(a) shows a Fermi surface (FS) map obtained by integrating ARPES intensity inside a 20-meV energy window around the Fermi energy (E_F), measured with photon energy 7 eV. There are three distinct regions with high photoemission intensities: a 3D FS centered at the Γ point (α), a small 2D hole pocket along the Γ-X line (β), and a skinny 2D banana-like pocket on the Γ-M line (γ). To compare the data with the calculation, we plot the Fermi surface as calculated by DFT in Fig. 3(b). This calculation shows all three of these features. The lack of fourfold symmetry in the data [Fig. 3(a)] as compared with the calculated FS [Fig. 3(b)] is due to selection rules arising from the photon polarization.

Figure 3(c) shows the photon-energy-dependent k maps from 50–120 eV of the ARPES intensity at E_F, cut along the Γ-X high-symmetry line [yellow dashed line in Fig. 3(a)]. The Fermi-edge k_x-k_z photon-energy-dependent maps show 2D behavior for the X-point pocket (β) but 3D k_z-dispersive behavior near the Γ point (pocket α). These features are reported in related compounds: The 2D state was observed in $YbMnBi_2$ [8], which was attributed to the Yb-Bi plane, and 3D behavior has been reported in $LaAgSb_2$ and attributed to the Sb plane [23].

ARPES intensity plots along the M-Γ-M and X-Γ-X lines are shown in Fig. 4. The calculated bands in each cut are overlaid on the ARPES data to show the robust agreement between the experiment and the calculation. Note the presence of a hole pocket in Fig. 4(a) and an electron pocket in Fig. 4(b), both with linear dispersion.

E. Transport and Hall effect

Single crystals were contacted by sputtering gold in the desired configuration and attaching annealed platinum wires with silver paste (Dupont 4929N). After contacting, the sample was shaped into a "Hall bar" geometry using a plasma focused ion beam (FIB), with the current injected parallel to the

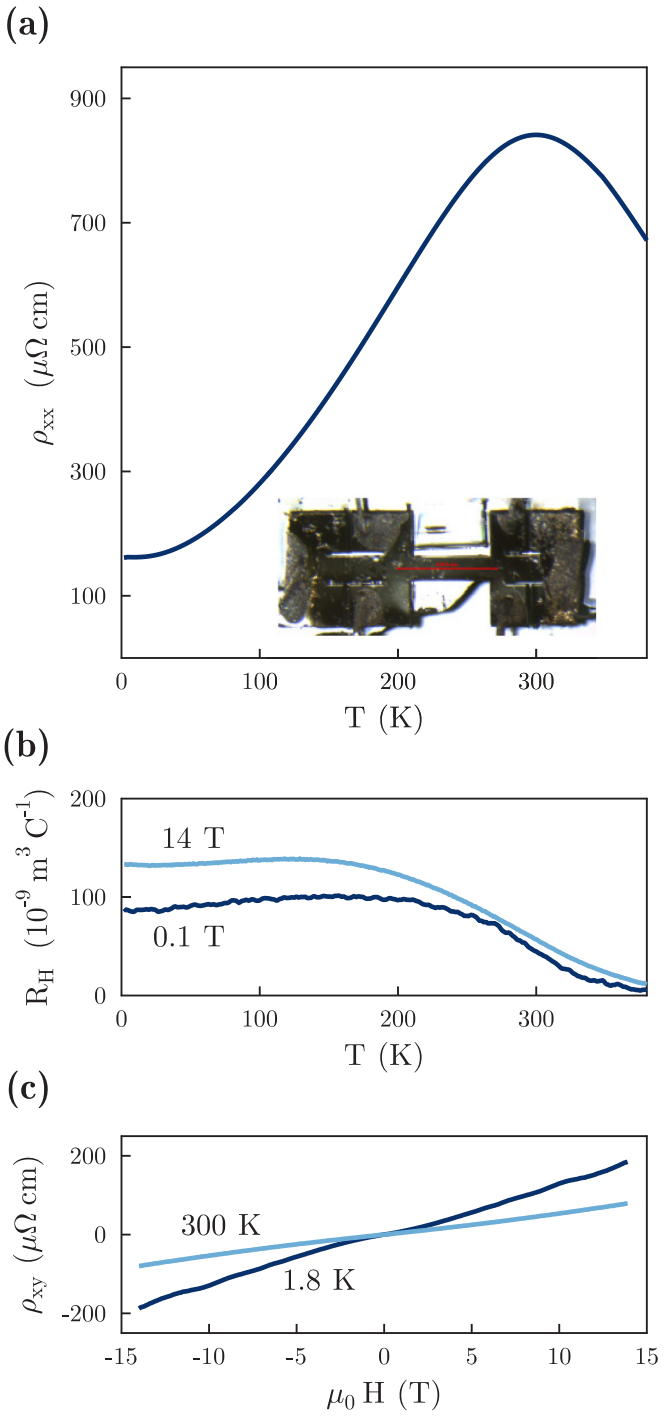

FIG. 5. Magnetotransport and heat capacity of $YbMnSb_2$. (a) Resistivity versus temperature. Inset: "Hall bar" sample geometry prepared using plasma FIB etching. (b) Hall coefficient (R_H) versus temperature measured at ± 0.1 T and ± 14 T. (c) ρ_{xy} versus magnetic field, antisymmetrized with respect to field polarity, at 1.8 K and 300 K.

crystallographic a axis. The Hall effect was measured with the magnetic field parallel to the c axis [out of the page in Fig. 5(a) inset]. The resistance and magnetoresistance measurements were performed in a Quantum Design Physical Properties Measurement System (PPMS).

Figure 5(c) shows ρ_{xx} as a function of temperature. The nonmonotonic temperature dependence of the resistivity could indicate a crossover between metallic and semiconducting behavior. It is unclear that this peak is associated with a true phase transition as its position varies between samples by over 20 K. The plot of Hall coefficient [Fig. 5(b)] as a function of temperature was constructed by antisymmetrizing data at ± 0.1 T and ± 14 T. The latter trace captures the high-field Hall coefficient, and the former trace approximately reflects the low-field Hall coefficient. Above $T \gtrsim 250$ K, nonlinearity in the Hall effect has vanished and the two traces converge.

At high fields ($\omega_c \tau \gg 1$), the Hall coefficient of a multiband system is inversely related to the degree of compensation, according to

$$(eR_H)^{-1} \equiv n_\infty = n_h - n_e, \tag{1}$$

where n_h is the total hole density and n_e is the total electron density [24]. We observe a reduction of the Hall coefficient with increasing temperature, which could reflect a reduction in the degree of compensation (assuming the high field limit is reached by 14 T, at 1.8 K, $n_\infty \sim 4.7 \times 10^{19}$ cm^{-3} while at 390 K $n_\infty \sim 7.5 \times 10^{20}$ cm^{-3}). However, it is likely that the high field limit is not reached at high temperatures, so this change arises from a combination of the availability of thermally excited carriers and changing mobilities of electron and hole pockets.

A simple two-band low-field form of the effective carrier density predicts that this effective carrier density is dominated by high mobility carriers, according to

$$(eR_H)^{-1} \equiv n_0 = \frac{(n_h \mu_h + n_e \mu_e)^2}{n_h \mu_h^2 - n_e \mu_e^2}, \tag{2}$$

where μ_i is each carrier's respective mobility. Band structure and photoemission both indicate that three bands may be present at the Fermi level, but qualitatively this two-band model shows that the Hall coefficient is determined by the highest mobility carrier. At low temperature, then, the 0.1-T trace (representing the low-field limit) shows the presence of high-mobility holes.

F. Shubnikov–de Haas measurements

We observed Shubnikov–de Haas (SdH) oscillations in magnetic fields of up to 14 T at temperatures between 1.8 K and 35 K. Our results (Fig. 6) indicate that the Fermi surface is small (perpendicular area approximately 0.1% of the bulk Brillouin zone) and strongly anisotropic, and the effective mass is small ($\mu = m^*/m_e = 0.1$).

Raw resistance versus field traces are processed in several steps. First, we subtract a best-fit fourth-order polynomial background from the trace. (For the frequencies observed, the results are largely insensitive to the order of polynomial background subtracted.) Our background-subtracted traces are plotted against inverse field ($1/\mu_0 H$) in Fig. 6(a). The background-free data are Fourier transformed against the inverse field to confirm the oscillation frequency.

In the absence of magnetic breakdown and other high-field effects, the oscillation frequencies observed are proportional to the areas of extremal orbits on the Fermi surface, in the plane

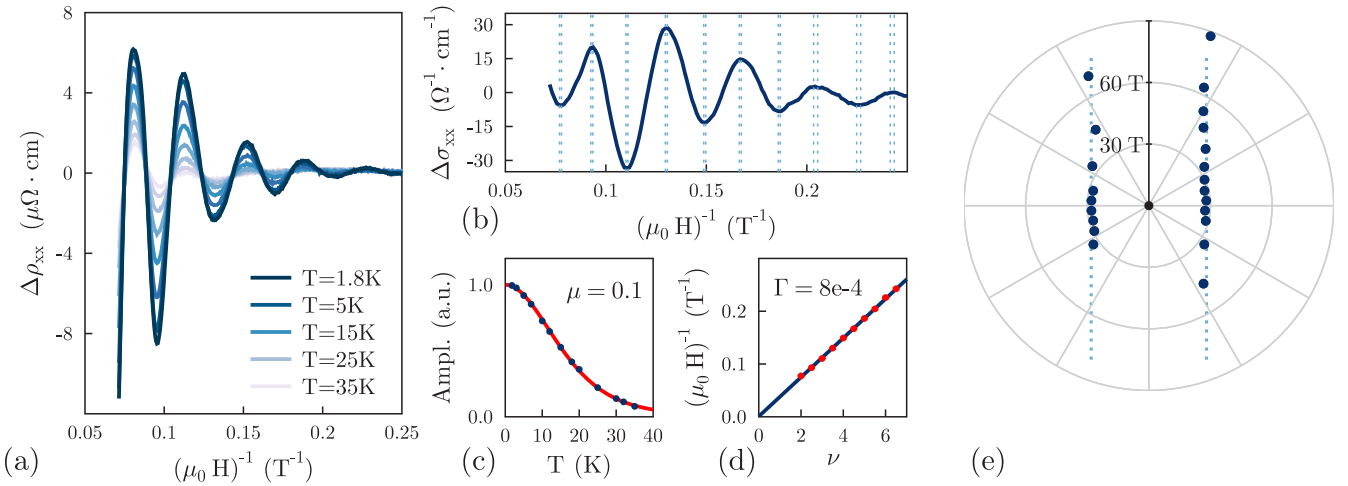

FIG. 6. Shubnikov–de Haas oscillations in $YbMnSb_2$. See also Table III. (a) Background-subtracted resistivity oscillations as a function of inverse field. The oscillation frequency is (28 ± 1) T, corresponding to an orbital area of 2.8×10^{-3} Å^{-2} [Eq. (3)]. (b) Longitudinal conductivity, σ_{xx}, plotted against inverse field. Dashed lines indicate the uncertainty in identifying the peak locations. Minima in the conductivity mark integer Landau levels crossing the Fermi surface. σ_{xx} is computed using Eq. (4). (c) Lifshitz-Kosevich (LK) [Eq. (5) Eq. (6)] fit to decay of the background-subtracted oscillation amplitude with temperature, with $\mu = 0.100 \pm 0.001$. Blue markers indicate oscillation amplitudes, and the red curve is the LK fit. (d) Landau fan diagram with linear fit. Using Eq. (9), the most likely ϕ_B is $(0.9984 \pm 0.003)\pi$ with the error bars computed from the fit error. (e) Polar plot of angular dependence of oscillation frequency. Dark blue markers indicate oscillation frequencies at different angles, as determined via Fourier transform of the background-subtracted oscillations. At zero degrees, the current flows (and voltage is measured) along the a axis and the field is aligned with the c axis. At 90°, the field and current are parallel to the a-axis. The dispersion of the oscillation frequency with angle is consistent with a two-dimensional Fermi surface, which would disperse as $1/\cos(\theta)$ (dashed lines). Above 75°, the oscillation amplitude becomes too small to track.

normal to the applied field. Explicitly,

$$F = \frac{\hbar}{2\pi e} S_e, \tag{3}$$

where F is the oscillation frequency and S_e the (k-space) extremal area.

The SdH effect appears intrinsically as an oscillatory component of the conductivity, which we are able to obtain by simultaneous measurements of Hall and longitudinal resistance. Then σ_{xx} can be calculated according to

$$\sigma_{xx} = \frac{\rho_{xx}}{\rho_{xx}^2 + \rho_{xy}^2} \tag{4}$$

and is shown in Fig. 6(b).

The SdH oscillation amplitude decays with temperature according to the Dingle form

$$R_T = \frac{x}{\sinh(x)}, \tag{5}$$

with

$$x = \left(2\pi^2 \frac{k_B m_e}{\hbar e}\right) p\mu T/B. \tag{6}$$

Here p is the harmonic index of the specific oscillation, μ is the cyclotron effective mass in units of the electron mass, T and B are the temperature and magnetic field, and m_e is the bare electron mass [25].

In Fig. 6(c) we fit our data to Eq. (5), including a small offset arising from imperfect background subtraction, and we find that $\mu = 0.100 \pm 0.001$. (The amplitude plotted is the amplitude of the peak at approximately 10.45 T after background subtraction.) This mass is comparable to that observed in other topological systems, including Cd_3As_2 [26], TaAs [27], and Na_3Bi [28].

The SdH oscillation amplitude also decays with $1/B$ due to the effect of finite carrier relaxation times according to the formula

$$R_D = \exp(-xT_D/T), \tag{7}$$

where T_D is called the Dingle temperature and is inversely related to the relaxation time [29].

$$\tau_D = \frac{\hbar}{2\pi k_B} \frac{1}{T_D} \tag{8}$$

Combining the 28 ± 1 T oscillation frequency in Fig. 6(a) with the effective mass from Fig. 6(b) allows us to compute the various values in Table III. Our reported oscillation frequency represents a Fermi-surface cross-sectional area of only 0.1% of the perpendicular Brillouin zone area $(2\pi/a)^2 = 2.1$ Å^{-2}.

TABLE III. Electronic properties from Shubnikov–de Haas oscillations. Here F is the SdH frequency, k_F is the Fermi wave number, m_c is the cyclotron mass, n_{SdH} is the carrier density, and T_D is the Dingle temperature.

Parameter	Value
F (T)	28 ± 1
k_F (nm^{-1})	0.29 ± 0.01
m_c (m_e)	0.100 ± 0.001
n_{SdH} (cm^{-3})	$(5.0 \pm 0.1) \times 10^{19}$
T_D (K)	23 ± 2

The so-called Landau level fan diagram is frequently employed to measure the Berry's phase in suspected topological systems. Conductivity minima in SdH oscillations [Fig. 6(b)] are plotted against their associated Landau level index. The x intercept of a linear fit to these data identifies the phase of the oscillations, and, in principle, the Berry's phase accumulated around one cyclotron orbit, according to the relation

$$\Gamma = \frac{1}{2} - \frac{\phi_B}{2\pi} + \delta, \tag{9}$$

in which Γ is the x intercept, ϕ_B the Berry's phase, and δ a number less than $1/8$ in magnitude [30–34]. Some authors suggest that δ is related to Fermi surface curvature: a smooth, 2D cylinder yields $\delta = 0$, but a "corrugated 3D Fermi surface" merits $|\delta| = 1/8$ [33]. The angular dependence of the oscillation frequency [Fig. 6(e) and discussed below] indicates our system is close to the 2D cylinder case, suggesting $\delta \approx 0$. In this case, a topologically nontrivial Berry's phase of π yields $\Gamma = 0$, while a trivial Berry's phase of 0 yields $\Gamma = 1/2$. The actual value we measure in Fig. 6(d) is $\Gamma = 8 \times 10^{-4} \pm 1.5 \times 10^{-3}$. This value indicates that the Fermi surface pocket we probe with SdH oscillations is consistent with having a topological origin.

By measuring SdH oscillations at different angles of the applied field, we are able to use the angular variation of the oscillation frequency to map the shape of the Fermi surface. The angular dependence of the SdH frequency is shown in Fig. 6(e), with a 5° sample positioning error subtracted. (After about 75° the oscillation amplitude has decreased in amplitude beyond detection.) Note that for a spherical Fermi surface, the data points in Fig. 6(e) would fall on a circle. Instead, they more closely follow a $1/\cos(\theta)$ dependence consistent with a two-dimensional or strongly anisotropic three-dimensional Fermi surface.

III. DISCUSSION

The angular dependence of the Shubnikov-de Haas oscillation frequency is consistent with a small 2D Fermi surface. This result is commensurate with our ARPES measurements, which show small 2D pockets along the $(0,\pi)$ and (π,π) directions in the Brillouin zone. Moreover, both ARPES and the Landau level fan diagram suggest that these pockets originate from a Dirac band crossing. $YbMnSb_2$ may therefore be a new topological material.

ARPES and DFT calculations indicate that three Fermi surface pockets contribute carriers: (1) small 3D holelike pockets (α) with a large effective mass, (2) 2D electron-like cylinders (β) with a small effective mass, and (3) small 2D holelike elliptic cylinders (γ), also with a small effective mass.

Using the SdH oscillation data in Table III, we can place an upper bound on the low temperature resistivity with a simple Drude approximation for a single pocket. This value is an upper bound both because the Dingle lifetime is sensitive to small-angle scattering (which only weakly affects the resistance) and because it ignores all other Fermi pockets [29]. Assuming a cylindrical Fermi surface, this bound is 133 ± 13 $\mu\Omega$cm, with the uncertainty primarily arising from the determination of the Dingle lifetime. Our observed resistivity at low temperature is 160 ± 16 $\mu\Omega$cm, which nearly coincides with this upper bound. (The uncertainty in this resistivity originates from the measurement of the sample thickness.) This observation would imply that $YbMnSb_2$ is in an unusual case whereby the quantum lifetime matches the transport lifetime. There are two plausible explanations for this. The first is that the quantum oscillations we observe do not originate from bulk bands but in fact originate from high mobility surface states that carry most of the current. However, our preliminary studies show that there is a weak thickness dependence to the resistivity, suggesting that surface states do not contribute significantly to the current.

The second scenario is that, although the quantum (Dingle) lifetime tends to underestimate the transport (Drude) lifetime due to its sensitivity to small-angle scattering, the Fermi surface in this material is quite small and so small-angle scattering may be catastrophic and, hence, efficiently dissipating momentum. The remainder of the carriers must then have very low mobility and contribute relatively little to conduction having been "shorted out" by the mobile carriers observed in quantum oscillations. In this scenario, the SdH oscillations must originate from either the 2D β or γ pockets since the α pockets can be ruled out because they are 3D. The Hall effect [Fig. 5(c)] indicates that holelike carriers are more numerous and more mobile, suggesting the γ pocket is the origin of these oscillations. On the other hand, the balance of carriers and mobilities may conspire to achieve an identical Hall signal such that the β pockets cannot be ruled out. In essence, the similarity between the 2D β and γ pockets prevents us from conclusively identifying either as the source of the SdH oscillations. Nevertheless, the balance of evidence suggests this second scenario most likely explains our data.

Finally, we emphasize that our ARPES data cannot be reconciled with our DFT calculations without antiferromagnetic order on the Mn sites. Thus, although we do not have any direct thermodynamic evidence for an antiferromagnetic phase transition, the close agreement between the calculations and experiment strongly suggests the presence of magnetic order. It may be that the thermodynamic anomaly is weak and cannot be resolved or occurs at temperatures beyond those measured here. Compounds with identical Mn sublattices, including $EuMnBi_2$ ($T_N \approx 310$ K) [4] and $SrMnBi_2$ ($T_N \approx 290$ K) [35], exhibit antiferromagnetic ordering near room temperature.

IV. CONCLUSION

We have performed a comprehensive study of the candidate topological semimetal $YbMnSb_2$ using electrical transport and ARPES measurements, all of which can be reconciled with our detailed DFT calculations. Shubnikov–de Haas oscillations reveal a 2D Fermi surface of Dirac origin, as predicted by DFT and consistent with ARPES measurements. This work indicates that $YbMnSb_2$ is a possible new test bed for the study of topological states of matter in the presence of broken-symmetry order.

ACKNOWLEDGMENTS

R.K. is supported by the National Science Foundation (NSF) Graduate Research Fellowship under Grant No. DGE-1106400. S.J., C.J., J.G.A., and much of this work received

support from the Gordon and Betty Moore Foundation under Grant No. GBMF4374. R.K., C.J., S.D., and J.G.A. also acknowledge the support from the NSF under Grant No. 1607753. S.J., S.M.G., J.D.D., and J.B.N. were supported by the Director, Office of Science, Office of Basic Energy Sciences, Materials Sciences and Engineering Division, of the U.S. Department of Energy under Contract No. DE-AC02-05-CH11231. Computational resources provided in part by the Molecular Foundry were supported by the Office of Science, Office of Basic Energy Sciences, of the U.S. Department of Energy, also under Contract No. DE-AC02-05-CH11231. S.M.G. acknowledges financial support by the Swiss National Science Foundation Early Postdoctoral Mobility Program. K.A.B. and J.Y.C. acknowledge partial support from NSF DMR-1360863. This paper also benefited from Dr. Nicholas P. Breznay's constructive feedback.

[1] K. Wang and C. Petrovic, Phys. Rev. B **86**, 155213 (2012).
[2] Y. F. Guo, A. J. Princep, X. Zhang, P. Manuel, D. Khalyavin, I. I. Mazin, Y. G. Shi, and A. T. Boothroyd, Phys. Rev. B **90**, 075120 (2014).
[3] Y. J. Jo, J. Park, G. Lee, M. J. Eom, E. S. Choi, J. H. Shim, W. Kang, and J. S. Kim, Phys. Rev. Lett. **113**, 156602 (2014).
[4] A. F. May, M. A. McGuire, and B. C. Sales, Phys. Rev. B **90**, 075109 (2014).
[5] M. A. Farhan, G. Lee, and J. H. Shim, J. Phys.: Condens. Matter **26**, 042201 (2014).
[6] J. Y. Liu, J. Hu, Q. Zhang, D. Graf, H. B. Cao, S. M. A. Radmanesh, D. J. Adams, Y. L. Zhu, G. F. Cheng, X. Liu, W. A. Phelan, J. Wei, M. Jaime, F. Balakirev, D. A. Tennant, J. F. DiTusa, I. Chiorescu, L. Spinu, and Z. Q. Mao, Nat. Mater. **16**, 905 (2017).
[7] A. A. Zyuzin, S. Wu, and A. A. Burkov, Phys. Rev. B **85**, 165110 (2012).
[8] S. Borisenko, D. Evtushinsky, Q. Gibson, A. Yaresko, T. Kim, M. N. Ali, B. Büchner, M. Hoesch, and R. J. Cava, arXiv:1507.04847 [cond-mat].
[9] Z. Wang, M. G. Vergniory, S. Kushwaha, M. Hirschberger, E. V. Chulkov, A. Ernst, N. P. Ong, R. J. Cava, and B. A. Bernevig, Phys. Rev. Lett. **117**, 236401 (2016).
[10] A. Wang, I. Zaliznyak, W. Ren, L. Wu, D. Graf, V. O. Garlea, J. B. Warren, E. Bozin, Y. Zhu, and C. Petrovic, Phys. Rev. B **94**, 165161 (2016).
[11] J. Liu, J. Hu, H. Cao, Y. Zhu, A. Chuang, D. Graf, D. J. Adams, S. M. A. Radmanesh, L. Spinu, I. Chiorescu, and Z. Mao, Sci. Rep. **6**, 30525 (2016).
[12] S. Huang, J. Kim, W. A. Shelton, E. W. Plummer, and R. Jin, Proc. Natl. Acad. Sci. USA **114**, 6256 (2017).
[13] G. M. Sheldrick, Acta Crystallogr. A **71**, 3 (2015).
[14] G. M. Sheldrick, Acta Crystallogr. C **71**, 3 (2015).
[15] K. Momma and F. Izumi, J. Appl. Crystallogr. **44**, 1272 (2011).
[16] L. Andrukhiv, L. Lysenko, Y. Yarmolyuk, and E. Gladyshevskii, Dop. Akad. Nauk Ukrain. RSR A **1975**, 645 (1975).
[17] P. Wollesen, W. Jeitschko, M. Brylak, and L. Dietrich, J. Alloys Compd. **245**, L5 (1996).
[18] G. Kresse and J. Furthmüller, Phys. Rev. B **54**, 11169 (1996).
[19] G. Kresse and J. Hafner, Phys. Rev. B **48**, 13115 (1993).
[20] H. J. Monkhorst and J. D. Pack, Phys. Rev. B **13**, 5188 (1976).
[21] J. P. Perdew, K. Burke, and M. Ernzerhof, Phys. Rev. Lett. **77**, 3865 (1996).
[22] S. L. Dudarev, G. A. Botton, S. Y. Savrasov, C. J. Humphreys, and A. P. Sutton, Phys. Rev. B **57**, 1505 (1998).
[23] X. Shi, P. Richard, K. Wang, M. Liu, C. E. Matt, N. Xu, R. S. Dhaka, Z. Ristic, T. Qian, Y.-F. Yang, C. Petrovic, M. Shi, and H. Ding, Phys. Rev. B **93**, 081105 (2016).
[24] M. Kohler, Ann. Phys. **440**, 99 (1949).
[25] I. M. Lifshitz and L. M. Kosevich, J. Exp. Theor. Phys. **6**, 67 (1958).
[26] L. P. He, X. C. Hong, J. K. Dong, J. Pan, Z. Zhang, J. Zhang, and S. Y. Li, Phys. Rev. Lett. **113**, 246402 (2014).
[27] C.-L. Zhang, Z. Yuan, Q.-D. Jiang, B. Tong, C. Zhang, X. C. Xie, and S. Jia, Phys. Rev. B **95**, 085202 (2017).
[28] S. K. Kushwaha, J. W. Krizan, B. E. Feldman, A. Gyenis, M. T. Randeria, J. Xiong, S.-Y. Xu, N. Alidoust, I. Belopolski, T. Liang, M. Z. Hasan, N. P. Ong, A. Yazdani, and R. J. Cava, APL Materials **3**, 041504 (2015).
[29] D. Shoenberg, *Magnetic Oscillations in Metals*, Cambridge Monographs on Physics (Cambridge University Press, Cambridge, 1984).
[30] P. Sergelius, J. Gooth, S. Bäßler, R. Zierold, C. Wiegand, A. Niemann, H. Reith, C. Shekhar, C. Felser, B. Yan, and K. Nielsch, Sci. Rep. **6**, 33859 (2016).
[31] I. A. Luk'yanchuk and Y. Kopelevich, Phys. Rev. Lett. **97**, 256801 (2006).
[32] J. Cao, S. Liang, C. Zhang, Y. Liu, J. Huang, Z. Jin, Z.-G. Chen, Z. Wang, Q. Wang, J. Zhao, S. Li, X. Dai, J. Zou, Z. Xia, L. Li, and F. Xiu, Nat. Commun. **6**, 7779 (2015).
[33] I. A. Luk'yanchuk and Y. Kopelevich, Phys. Rev. Lett. **93**, 166402 (2004).
[34] A. Pariari, P. Dutta, and P. Mandal, Phys. Rev. B **91**, 155139 (2015).
[35] J. Park, G. Lee, F. Wolff-Fabris, Y. Y. Koh, M. J. Eom, Y. K. Kim, M. A. Farhan, Y. J. Jo, C. Kim, J. H. Shim, and J. S. Kim, Phys. Rev. Lett. **107**, 126402 (2011).